


# Quantum Tunneling-induced Hybridization and Coherent Dynamics of Jackiw-Rebbi Zero Modes in a Modified Su-Schrieffer-Heeger Chain

Surajit Mandal<sup>1,2</sup> 

<sup>1</sup>*Department of Physics, Jadavpur University, Kolkata - 700032, West Bengal, India*

<sup>2</sup>*Department of Physics, AKPC Mahavidyalaya, Bengai - 712611, West Bengal, India*

We investigate analytically and numerically the tunneling-induced hybridization and coherent dynamics of Jackiw-Rebbi (JR) zero modes in a modified Su-Schrieffer-Heeger (SSH) model. Unlike the conventional SSH model, this modified system possess two bulk gap closing points, namely, the quadratic-type gap closing point at  $k = 0$  and the Dirac-type gap closing point at  $k = \pm\pi/4a$ . While the quadratic point does not support a topological domain wall due to the absence of mass inversion, the low-energy Dirac theory around  $k = \pm\pi/4a$  predicts an effective mass that changes sign at two spatially separated interfaces under a kink profile, generating a pair of JR bound states localized at those interfaces. We show that finite overlap between the JR zero modes lifts the zero-energy degeneracy through quantum tunneling, producing symmetric-antisymmetric hybridized states analogous to a quantum mechanical double-well system. An effective two-level description reveals coherent oscillations of the occupation probability between the two JR modes, accompanied by periodic transfer of sublattice polarization between the (A,C) and (B,D) sectors. The oscillation period is governed by the hybridization gap, providing a tunable route for controlling topological bound states. Our results establish a unified framework connecting JR zero modes, quantum tunneling, and coherent dynamics in modified SSH systems, offering a promising platform for controllable topological quantum-state transfer in engineered lattice structures.

## I. INTRODUCTION

The discovery of localized zero-energy states (ZESs) bound to topological defects represents one of the most profound developments at the interface of quantum field theory and condensed-matter physics[1]. In 1976, a seminal work by Jackiw and Rebbi demonstrated that a one-dimensional (1D) massive Dirac fermion coupled to a space-dependent soliton mass field can support a topological boundary state, familiar as the Jackiw-Rebbi modes (JRM), at the mass domain wall[1] and this JRM can show fractional charge excitations[1–5]. Nowadays, the exploration of JRMs, due to their exotic excitation with fractional charge, has enticed a large attraction in modern condensed matter systems. In particular, they can be a feasible candidate for performing topological quantum computation[6]. Moreover, the JRMs subsequently emerged as a paradigmatic example of a topological defect state and have found manifestations in a wide range of physical systems, including conducting polymers[7, 8], topological insulators[9, 10], photonic lattices[11, 12], as well as photonic and acoustic metamaterials[13–16]. More recently, the realization of JRMs has been extended beyond lattice systems to non-uniform topological insulator nanowires with external magnetic flux[17].

The most popular condensed-matter realization of the JRMs is provided by the Su-Schrieffer-Heeger (SSH) model, which was originally introduced in the context of soliton excitations in polyacetylene. Owing to its chiral symmetry and dimerized structure, the model re-

sults in two degenerate ground states[8, 18, 19]. A domain wall connecting regions with opposite dimerized phases acts as a lattice analogue of the mass kink in the Jackiw-Rebbi (JR) problem and hosts exponentially localized midgap ZESs. The SSH model has therefore become a cornerstone in the study of 1D topological phases, offering a simple yet powerful platform to explore the interplay between symmetry, topology, and localized quantum states[20–22]. The outcome of having static domain walls (DWs) at an interface of the SSH chain[24] and some other models[25–27] has been probed to some extent in the literature.

In this respect, it would be ludicrous to add here that the domain-wall bound state for the original SSH model can be understood from the low-energy Dirac theory, obtained by expanding the Bloch Hamiltonian around the Dirac-type critical momentum  $k = \pi$ , where the bulk gap closes at the topological phase transition[28]. The resulting sign reversal of the Dirac mass across the interface[28] or changing hopping pattern at the interface[29, 30] gives rise to a localized JR zero mode. In contrast, the present model possess both a quadratic-type band-touching point at  $k = 0$  and Dirac-type critical points at  $k = \pm\pi/4$ . In the pertinent study documented in Ref. [29], the authors numerically examined the emergence of ZESs at the DW position for different commensurate frequencies. They found that for  $\theta = \pi/2$  (corresponding to the modified SSH model considered in the present work, to be discussed later), no ZESs can emerge at the DW location. Instead, they remain localized at the two ends of the finite chain. Although this intriguing result was reported numerically, its physical origin was left unexplained. In the present work, we provide a clear theoretical understanding of the same. Specifically, we analytically show that the effective mass obtained by expanding the Bloch

---

\* surajitmandalju@gmail.com; <https://orcid.org/0000-0002-9091-0539>

Hamiltonian around the quadratic point ( $k = 0$ ) does not undergo a topological sign inversion under the kink profile and therefore cannot support a JRM in this regime. Thus, in Ref.[29], the authors numerically studied the system in the parameter regime corresponding to the absence of mass inversion at the quadratic band-touching point. We further present a detailed analysis of the conditions under which JRMs can emerge within the DW region. In this context, we analytically show that expanding the same Bloch Hamiltonian around the Dirac critical points ( $k = \pm\pi/4$ ) yields an effective Dirac mass that undergoes two successive sign inversions near the chain center, giving rise to the formation of two interfaces or DWs capable of supporting two zero-energy JRMs. Additionally, we study the same by numerical diagonalization of the real-space Hamiltonian, which reveals localized zero-energy JRMs exclusively in the parameter regime characterized by mass inversion at the Dirac-type transition points.

However, the interplay between topology and quantum tunneling has attracted increasing attention across various physical settings in recent years. For example, the controllable tunneling-induced topological defect modes have been realized and manipulated in photonic, cold-atom, acoustic, and mechanical SSH-type lattices, where DWs and localized states can be engineered with high precision[11, 31–34]. Furthermore, the hybridization and coherent coupling of topological bound states have emerged as central themes in studies of Majorana modes and related topological excitations, highlighting the broader relevance of tunneling-induced energy splitting in topological matter and quantum information platforms[22, 35–39]. In all these cases, energy splitting serves as a sensitive probe of the overlap between topological states and sets the characteristic timescale for coherent quantum dynamics. Nevertheless, most previous studies have focused on conventional SSH chains or Majorana systems, while the tunneling dynamics of JRMs in the modified SSH model remains largely unexplored.

Motivated by these developments, we investigate the hybridization due to quantum tunneling and tunneling dynamics of JRMs in a modified SSH chain by analyzing the effective two-state Hamiltonian. We demonstrate that the overlapped JRMs localized at topological DWs form a topological analogue of a quantum-mechanical double-well system, where exponentially weak tunneling transforms two degenerate zero modes into bonding and antibonding states with finite energy splitting[40, 41, 43]. Remarkably, quantum tunneling in double-well potentials provides one of the most fundamental paradigms for understanding coherent dynamics in two-level quantum systems[44–46]. The phenomenon underlies a broad range of physical processes spanning vastly different length scales, from microscopic examples such as the inversion dynamics of the ammonia molecule[47] and electron transfer between coupled quantum dots[48] to macroscopic manifestations including Josephson oscillations in Bose–Einstein condensates[49–52] and quantum

tunneling in superconducting quantum interference devices (SQUIDs)[53–56]. Owing to its universal nature, the double-well problem continues to serve as a cornerstone for exploring quantum coherence, tunneling-induced level splitting, and nonequilibrium dynamics in complex quantum systems.

Using both analytical continuum theory and exact numerical lattice diagonalization, we investigate the dependence of the splitting energy on the DW amplitude, DW separation and width of DW, revealing an exponential scaling characteristic of quantum tunneling. We further investigate the coherent tunneling dynamics associated with the hybridized JRMs and show how the resulting oscillatory behavior, analogous to Rabi oscillations in a two-level system[57, 58], provides a direct dynamical signature of tunneling between topological JRMs.

Crucially, our results reflect that the two JRMs bound together by quantum tunneling form a two-level topological system that may be viewed as “*Jackiw-Rebbi molecule*”. This picture is directly analogous to the tunneling of quantum particles between the minima of a double-well potential and to the formation of bonding and antibonding molecular orbitals in the molecular ion  $H_2^+$ , where tunneling lifts the degeneracy of two localized states and generates a finite energy splitting[40–42, 59]. Moreover, our work reveals how concepts originating from relativistic quantum field theory, topological band theory, and elementary quantum tunneling converge within a single framework. Beyond elucidating the microscopic mechanism responsible for the lifting of topological zero-mode degeneracy, the results provide a route toward controllable manipulation of defect-bound states in engineered topological systems[11, 31–34] and establish modified SSH chains as a versatile platform for studying coherent quantum dynamics of topological excitations and their hybridization through tunneling[22, 35–37].

The paper is organized as follows. In Section II, we present a brief introduction to the modified SSH chain. This section also includes the phase transition of this modified SSH system. Section III discuss about the zero-energy JRMs both analytically and numerically. This section shows the existence of zero-energy JRMs for sufficiently large interface separation and also illustrates how JR zero modes become near zero-energy hybridized JRMs, via quantum tunneling, for finite interface separation. In Section IV, we study the coherent tunneling dynamics of hybridized JRMs via real-time evolution. Finally, in Section V, we summarize and conclude our findings and discuss possible future directions and applications of our work.

## II. MODIFIED SSH CHAIN

The Hamiltonian for the 1D SSH chain of  $L = M * N$  (in which  $M$  and  $N$  denote the number of sublattices and unit cells, respectively) sites with periodically modulated hopping strength can be defined, under open boundary

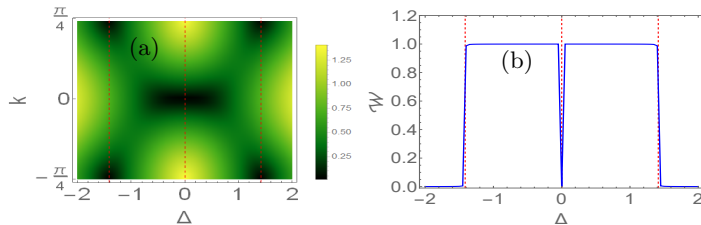


FIG. 1. (a) **Bulk gap closing** in  $(\Delta - k)$ - parameter space. (b) The variation **bulk winding number** with  $\Delta$ . Here, the vertical red dashed line indicates the location of the Dirac-type gap closing point at  $|\Delta/t| = \sqrt{2}$  and quadratic-type gap closing point at  $\Delta = 0$ .

conditions (OBC), as[29, 60]:

$$\mathcal{H}_{SSH} = \sum_i^{L-1} (t + \delta_i)[|i\rangle \langle i+1| + H.c], \quad (1)$$

where  $\delta_i = \Delta \cos[(i-1)\theta]$  with  $i = 1, 2, 3, \dots, n$  specifies the periodic modulation in the nearest-neighbor hopping strength  $t$ . Generally, one obtains  $\delta_{i+1} = \Delta \cos(2\pi i/M)$  for a commensurate frequency  $\theta = \frac{2\pi}{M}$ . Therefore, the system is represented by a  $M \times M$  Hamiltonian matrix having  $M$  number of eigenmodes. Crucially, the commensurate frequencies such as  $\theta = \pi, \pi/2, \pi/3$  and  $\pi/4$  produce, respectively, the two, four, six, and eight sublattices in a unit cell, giving the increasing periodicity of the system for decreasing frequency. For the sake of simplicity, we consider  $t = 1$  as the unit of energy, which further makes the unit of physical parameter dimensionless throughout this work. However, all the parameters considered here are real.

We should mention here that the above model (Eq. (1)) for  $\theta = \pi$  corroborates with the original SSH model having two atom basis unit cells[18, 29, 60, 61]. However, the lattice periodicity increases twice for  $\theta = \pi/2$ , with the number of sublattices now becoming four. We shall discuss the rest of the physics by considering this four-sublattice basis SSH chain, called as the modified SSH model. Before studying the quantum tunneling, appearance of hybridized JRMs and coherent tunneling dynamics of these JRMs, we shall briefly discuss about the phase transition of this modified SSH model. To do so, the Bloch Hamiltonian in the  $k$ -space for the model under periodic boundary conditions (PBC) yields[29]

$$\mathcal{H}(k) = \begin{pmatrix} 0 & (t + \Delta) & 0 & te^{-4ik} \\ (t + \Delta) & 0 & t & 0 \\ 0 & t & 0 & (t - \Delta) \\ te^{4ik} & 0 & (t - \Delta) & 0 \end{pmatrix}, \quad (2)$$

Now, the dispersion relation turns out to be

$$E(k) = \pm \sqrt{2t^2 + \Delta^2 \pm t\sqrt{2t^2 + 6\Delta^2 + 2(t^2 - \Delta^2)\cos 4k}}, \quad (3)$$

thus, the bulk band touches at  $E(k) = 0$  for the momenta given by  $k = \pm \frac{1}{4} \arccos \left[ \frac{2t^2 - 2t^2\Delta^2}{2t^2(t^2 - \Delta^2)} \right]$ . Therefore, the bulk

energy gap closing point can be noticed not only at the boundary of reduced first Brillouin zone ( $k = \pm\pi/4$ ) at  $|\Delta/t| = \sqrt{2}$ , but also at the Brillouin zone center ( $k = 0$ ) for  $\Delta = 0$  (see Fig. 1(a)). The energy band gap is  $E_{gap} \sim |2t^2 - \Delta^2|$  at  $k = \pm\pi/4a$  for  $|\Delta/t| \neq \sqrt{2}$ , whereas it becomes  $E_{gap} \sim |\Delta|^2$  at  $k = 0$  when  $\Delta \neq 0$ . The former results in a Dirac-type linear band touching at  $|\Delta/t| = \sqrt{2}$  under both PBC and OBC, while the latter gives rise to a quadratic type gap closing exactly at  $\Delta = 0$  for the model under both PBC and OBC. It is exemplary that the Hamiltonian in Eq. (1) respects the chiral symmetry  $\{\Gamma_4, \mathcal{H}_k\} = 0$  with the chiral operator  $\Gamma_4 = \text{diag}\{1, -1, 1, -1\}$ . Additionally, the Hamiltonian also respects the particle-hole symmetry along with time reversal symmetry and falls in the BDI class in a tenfold way classification scheme[29, 62, 63]. Thus, the topology of the model can be characterized by the bulk topological invariant, winding number[64–67].

The bulk winding number changes on either side of  $|\Delta/t| = \sqrt{2}$ , leading to the visibility of “first-order” (as the modulation parameter  $\Delta$  enters linearly in  $E_{gap}$  or effective mass) non-trivial topological phase transition point only at  $k = \pm\pi/4a$ . On the other hand, the winding number does not change in the vicinity of the  $\Delta = 0$  point, reflecting it as a trivial metallic point due to a “second-order” (because  $\Delta$  enters quadratically in  $E_{gap}$ ) trivial topological phase transition. One can notice the non-trivial topological phase with  $\mathcal{W} = 1$  within the range  $0 < |\Delta/t| < \sqrt{2}$  while the trivial topological phase with  $\mathcal{W} = 0$  occurs when  $\Delta = 0$  or  $|\Delta/t| > \sqrt{2}$  (notice Fig. 1(b))[29]. Similar to the usual SSH chain ( $\theta = \pi$  case for Hamiltonian Eq. (1)), two ZES can be found here; however, unlike that scenario, this configuration also admits two mid-gap states having non-zero energy[29]. The features of the ZES have been previously studied in Ref.[29], which exhibit their edge localization.

We now consider the DW configuration and study the tunneling-induced hybridization of the JRMs, if any, in the following sections.

### III. STUDY OF ZERO ENERGY JACKIW-REBBI MODES

In this section, we seek to investigate the zero-energy JRMs, which, in the context of the SSH chain is one of the most beautiful and fundamental concepts in topological condensed matter physics. It represents a lattice-bound realization of a famous particle physics phenomenon: fractional quantum numbers and zero-energy bound states[2]. We should mention here that the topologically protected zero-energy JRMs can be discernible at the topological defect (rather, we can call it interface or DW from now on[69]), which can be created by changing the hopping arrangement at a certain lattice site or by flipping the fermion mass at a certain point[1–3, 29, 30]. The celebrated JR mode can be achieved both analytically and numerically, as discussed below. Specifically,

the analytical study is based on the continuum limit of the momentum-space Hamiltonian within the JR framework, while the numerical investigation is carried out by exact diagonalization of the corresponding real-space Hamiltonian.

### A. Analytical Study

For the analytical study, we utilize the JR method, which considers the continuum limit of the momentum-space Hamiltonian as discussed in Appendix A 1. Before proceeding further, we need to mention here that the present model includes both a quadratic band-touching point at  $k = 0$  and a Dirac-type critical point at  $k = \pm\pi/4$ . Now, expanding the Bloch Hamiltonian (Eq. (2)) around  $k = 0$  yields a position-dependent effective Dirac mass  $M(x) = -\Delta^2(x)$ , which does not change sign for a kink-type profile (Eq. (A1)) as shown in Fig. 2(a). Therefore, a topologically protected JRM is not expected at the DW position. The JRMs, instead, arise from the Dirac theories around  $k = \pm\pi/4$  as discussed below.

Due to the increased periodicity of the lattice here, we intend not only to see the intricate behavior of zero-energy JRMs but also to consider the sublattice polarization (microscopic structure) of those modes. To elucidate the microscopic structure of the JRMs, we need to define the Bloch Hamiltonian Eq. (2) in (A B C D)<sup>T</sup> basis and project this Hamiltonian onto the low-energy subspace at the Dirac-type linear gap closing point at  $k_c = \pm\pi/4a$ . Evaluating the Bloch Hamiltonian (Eq. (2)) at the critical point  $k_c$  provides the zero energy condition  $\mathcal{H}(k_c)u = 0$ , which results in two linearly independent eigenvectors as  $u_{AC} = C (1 \ 0 \ -(1 + \sqrt{2}) \ 0)^T$  and  $u_{BD} = C (0 \ 1 \ 0 \ (1 + \sqrt{2}))^T$  with  $C = [1 + (1 + \sqrt{2})^2]^{-1/2}$  is the normalization factor. Importantly, at the Dirac-type critical points  $k_c = \pm\pi/4a$ , the zero-energy eigenspace is twofold degenerate and naturally decompose into two orthonormal sectors  $u_{AC}$  and  $u_{BD}$ , which have support exclusively on the (A,C) and (B,D) sublattices, respectively. Projecting the lattice wavefunction onto the low-energy subspace spanned by  $u_{AC}$  and  $u_{BD}$ , the lattice wavefunction can therefore be expanded as

$$\Psi(x) = \phi_1(x)u_{AC} + \phi_2(x)u_{BD} \quad (4)$$

where the envelope amplitude defines the Dirac spinor  $(\phi_1(x) \ \phi_2(x))^T$ . Now, in order to apply the JR method of Appendix A 1, we first convert Eq. (2) into block off-diagonal form, which results in the following equation (see Appendix A 3 for more details)

$$\mathcal{H}(k) = h_x(k)\sigma_x + h_y(k)\sigma_y \quad (5)$$

In the continuum limit, performing a low description of Eq. (5) around  $k = \pm\pi/4a$  yields the effective Dirac

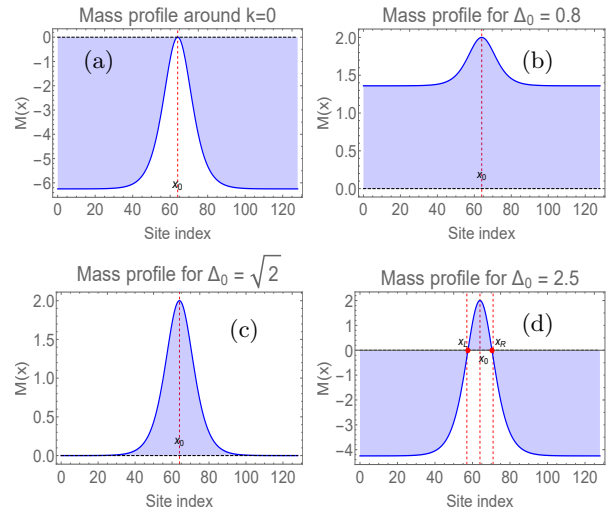


FIG. 2. The profile for effective Dirac mass,  $M(x) = -\Delta(x)^2$  around  $k = 0$  (a) and for effective Dirac mass  $M(x) = 2t^2 - \Delta_0^2 \tanh^2(\frac{x-x_0}{\xi/a})$  near  $k = \pm\pi/4$  with (b)  $\Delta_0 < \sqrt{2}t$ , (c)  $\Delta_0 = \sqrt{2}t$ , and (d)  $\Delta_0 > \sqrt{2}t$ . In (d),  $M(x)$  is not like the standard JR mass kink (Eq. (A1)), instead, it is symmetric about  $x_0$  producing two mass zeros at  $x_L$  and  $x_R$ , and it is like a double interface (kink-antikink pair) mass profile. Other parameters are  $L = 128$ ,  $\xi/a = 10$ .

Hamiltonian as

$$\mathcal{H}_{eff}(x) = M(x)\sigma_x - iv\sigma_y\partial_x + \mathcal{O}(x^2) \quad (6)$$

where the velocity becomes  $v = \frac{4at^2}{\hbar}$  and the spatially dependent effective Dirac mass  $M(x) = 2t^2 - \Delta^2(x)$ . Here, the DW profile is imposed on  $\Delta(x)$ , not directly on the Dirac mass. Following Eq. (A1), we define  $\Delta(x) = \Delta_0 \tanh(\frac{x-x_0}{\xi/a})$  and the Dirac mass to be  $M(x) = 2t^2 - \Delta_0^2 \tanh^2(\frac{x-x_0}{\xi/a})$ . For  $\Delta_0 < \sqrt{2}t$ ,  $M(x)$  does not change sign about the center of chain, while it changes sign twice in the vicinity of the chain center for  $\Delta_0 > \sqrt{2}t$ . Thus, two DW or interface are discernible at  $x_L = x_0 - x_*$  and  $x_R = x_0 + x_*$  with  $x_* = \frac{\xi}{a} \operatorname{arctanh}\left(\frac{\sqrt{2}t}{\Delta_0}\right)$ . Interestingly,  $M(x)$  just touches zero asymptotically for  $\Delta_0 = \sqrt{2}t$ , and indicates the bulk gap-closing point. For that, the interface positions move to infinity. We now present the mass profile for different values of  $\Delta_0$  in Fig. 2. Fig. 2(b) depicts no sign inversion, while Fig. 2(c) illustrates that the mass curve touches zero asymptotically. In contrast, Fig. 2(d) shows the appearance of two interfaces exactly at  $x_L$  and  $x_R$ . Importantly, the existence of two interfaces is analogous to the double-well potential in quantum mechanics[57]. Moreover, the barrier in the finite positive mass region  $x_L < x < x_R$  mimics the finite potential barrier in the double-well system[57].

Therefore, the search for ZESs here is essential because the inversion of the sign is noticed at the positions  $x_L$  and  $x_R$  for  $\Delta_0 > \sqrt{2}t$ . The ZESs, with domain wall configuration, come in pairs  $\pm E$  due to the preservation of chiral symmetry[28]. Now taking into account the linearized mass near each interface as  $M(x) = M'(x_j)(x - x_j)$ , Eq.

(6) reads

$$\mathcal{H}_j = M'(x_j)(x - x_j)\sigma_x - iv\sigma_y\partial_x \quad (7)$$

The zero-energy equation  $\mathcal{H}_j\phi_j = 0$  admits normalizable solutions only for a definite eigenvalue of  $\sigma_z$ . Writing  $\phi_j = f_j(x)\chi_s$  with  $\sigma_z\chi_s = s\chi_s$ ,  $s = \pm 1$ , one obtains envelope  $f_j(x) = \left(\frac{\alpha}{\pi}\right)^{1/4} \exp\left[-\frac{\alpha}{2}(x - x_j)^2\right]$  and the normalized solution estimated as

$$\phi_j(x) = \left(\frac{\alpha}{\pi}\right)^{1/4} \exp\left[-\frac{\alpha}{2}(x - x_j)^2\right]\chi_j \quad (8)$$

with  $\alpha = \frac{|M'(x_j)|}{v}$ ,  $j = L/R$  and the localization length being  $l = 1/\sqrt{\alpha}$ . While the solution with a '+' sign in the exponential blows up, which is not normalizable. The chirality of Eq. (8) can, however, be determined by the sign of the mass gradient  $s = \text{sgn}[M'(x_j)]$ . For the mass profile considered here,  $M'(x_L) > 0$  and  $M'(x_R) < 0$  which implies  $\chi_L = (1 \ 0)^T$  and  $\chi_R = (0 \ 1)^T$ . Transforming back to the microscopic lattice basis yields the interface states

$$\left. \begin{aligned} \Psi_L(x) &= f_L(x)u_{AC} \\ \Psi_R(x) &= f_R(x)u_{BD} \end{aligned} \right\} \quad (9)$$

It is evident from Eq. (9) that the mode  $\Psi_L(x)$  has an envelope  $f_L(x)$  that peaked at  $x_L$  and carries weight on the A and C sublattices. While  $\Psi_R(x)$  has an envelope  $f_R(x)$  that peaked at  $x_R$  and is entirely confined to the B and D sublattices. The states  $\Psi_L(x)$  and  $\Psi_R(x)$  are the zero modes obtained by solving the Dirac equation near each interface independently. Importantly, these two modes are independent DW modes (JRMs) having exact zero energy when the interfaces are far apart, i.e.,  $D_s (= x_R - x_L = 2x_*) \rightarrow \infty$ . To observe the localization behavior of the zero modes,  $\Psi_{L,R}(x)$ , we plot Fig. 3(a) which reveals the individual localization of  $\Psi_L(x)$  and  $\Psi_R(x)$  at the left interface  $x_L$  and right interface  $x_R$ , respectively, but a very negligible overlap between wavefunction tails is also visible in the intermediate positive mass region. This occurs because the separation  $D_s$  is much larger than the localization length  $l$ . As soon as we move towards  $\Delta_0 \rightarrow \sqrt{2}t^+$ , two peaks move infinitely far apart as  $x_* \rightarrow \infty$  and  $D_s \rightarrow \infty$ . Then the two modes would have strictly zero overlap, exactly like two bound states in two infinitely separated quantum wells[40, 41, 43].

**Quantum Tunneling, Energy splitting and Hybridized States:** Once the interface separation is finite, the two independent JRMs  $\Psi_L(x)$  and  $\Psi_R(x)$  can tunnel into each other and make a finite overlap, leading to nonzero tunneling matrix element  $T = \langle \Psi_L | \mathcal{H}_j | \Psi_R \rangle$ . Projecting the Dirac Hamiltonian  $\mathcal{H}_j$  into the  $\{\Psi_L, \Psi_R\}$  subspace, one obtains an effective two-state Hamiltonian, similar to the two-level Hamiltonian of a particle in a double well[43], as  $\mathcal{H}_{eff} = \begin{pmatrix} 0 & T \\ T^* & 0 \end{pmatrix}$  with eigenvalues

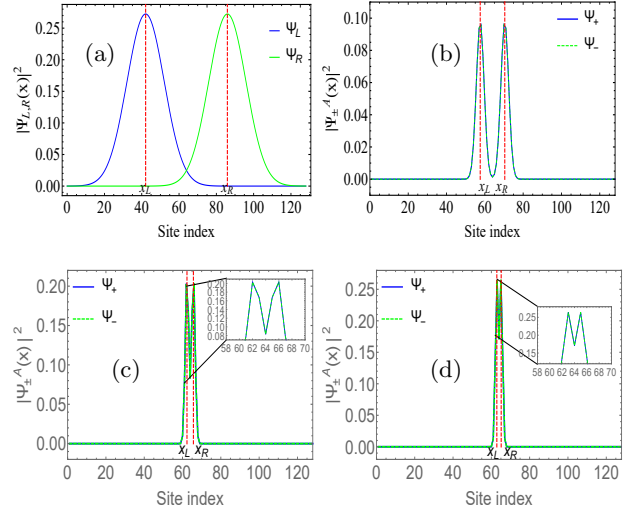


FIG. 3. **The analytical probability density of zero energy JRMs  $\Psi_{L,R}(x)$  (Eq. (9)) with  $\Delta_0 = 1.45$ ,  $D_s = 43.8248$  (a) and two hybridized JRMs  $\Psi_{\pm}(x)$  (Eq. (11) (b),(c),(d). In (b),  $\Delta_0 = 2.5$ ,  $D_s = 12.8231$ , (c)  $\Delta_0 = 8.5$ ,  $D_s = 3.35879$  while in (d)  $\Delta_0 = 12.5$ ,  $D_s = 2.27247$ . The figure shows that each peak is positioned at  $x_L$  and  $x_R$ . However, insets in panels (c) and (d) provide a magnified view of the exponential tails in the positive mass region, illustrating the enhanced overlap of the JRMs as the interface separation decreases. For each plot, we set  $L = 128$  and  $\xi/a = 10$ .**

$E_{\pm} = \pm|T|$  and  $\Delta E = \pm 2|T|$ . Thus, the degeneracy of zero modes is now being lifted. Within the overlap region  $\mathcal{H}_{eff} \sim \frac{v}{l}$ , overlap  $S = \langle \Psi_L | \Psi_R \rangle = e^{-\alpha x_*^2}$  and  $T \sim \frac{v}{l} e^{-\alpha x_*^2}$  with  $\alpha = \frac{|M'(x)|}{v}$  and  $l = \alpha^{-1/2}$ . Inserting  $v$ ,  $M'$ , we get

$$T = \sqrt{\frac{8\sqrt{2}\Delta_0 t^3}{\xi} \left(1 - \frac{2t^2}{\Delta_0^2}\right)} \exp\left[-\frac{\sqrt{2}\Delta_0}{2t\xi} \left(1 - \frac{2t^2}{\Delta_0^2}\right) x_*^2\right], \quad (10)$$

so for Gaussian envelope  $T \propto e^{-\frac{D_s^2}{(2l)^2}}$  and  $\Delta E \propto 2e^{-\frac{D_s^2}{(2l)^2}}$  with  $l$  becoming the localization length, while for large  $D_s$ , one can notice an asymptotic tail of the JRMs which results in  $T \propto e^{-\kappa D_s}$  and  $\Delta E \propto 2e^{-\kappa D_s}$  having localization length  $l_D = k^{-1}$  (notice Appendix B 1). To gain insight into the nature of energy splitting with DW separation  $D_s = 2x_*$  and DW amplitude, we plot Fig. 4. Specifically, Fig. 4(a) depicts that the energy splitting or tunneling matrix element is negligible near transition  $\Delta_0 \rightarrow \sqrt{2}t^+$ , and two JRMs are exact zero modes (Eq. (9)) as here two interfaces become infinitely far apart  $D_s \rightarrow \infty$  (see Fig. 4(b)).

For  $\Delta_0 > \sqrt{2}t$ ,  $x_* \simeq \frac{\xi}{a} \frac{\sqrt{2}t}{\Delta_0}$  and thus the two DWs approach each other, exhibiting their finite separation. Therefore, one can notice a finite tunneling matrix element, which permits the two independent JRMs to tunnel into each other, making a finite overlap. This results in a hybridization of two JRMs, producing a small energy splitting (notice Figs. 4(a) and (b)). The exact JRMs now become symmetric and antisymmetric combinations of  $\Psi_L(x)$  and  $\Psi_R(x)$ , and are given below

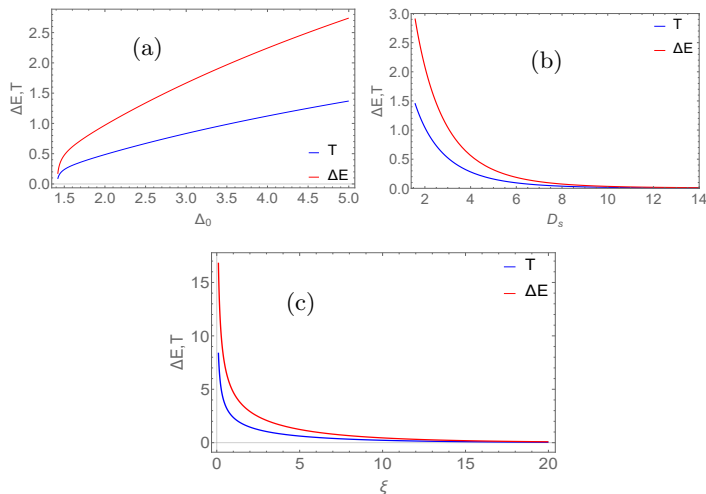


FIG. 4. **The tunneling matrix element and energy splitting** with respect to: (a) domain wall amplitude  $\Delta_0$ , (b) domain wall separation  $D_s = 2x_*$  and (c) domain wall width  $\xi$ .

$$\Psi_{\pm}(x) = \frac{\Psi_L(x) \pm \Psi_R(x)}{\sqrt{2}}, \quad (11)$$

This is identical to the bonding-antibonding states in double-well phenomenology in quantum mechanics[40–43]. Although  $\Psi_{\pm}(x)$  possess finite weight at both interfaces, their sublattice polarization remains spatially separated. Near  $x_L$ , where  $f_L(x_L) \gg f_R(x_L)$ , the JRMs are dominated by the (A,C) sector. In contrast, near  $x_R$ , where  $f_R(x_R) \gg f_L(x_R)$ , the JRMs reside predominantly in the (B,D) sublattices. To illustrate the behavior of  $\Psi_{\pm}(x)$  graphically, we plot Fig. 3(b), which exhibits weight at both interfaces along with finite tunneling in the intermediate region  $x_L < x < x_R$ .

As soon as  $\Delta_0 \gg \sqrt{2}t$ , the DW separation decreases as  $D_s \rightarrow 0$ . It can be observed from Figs. 4(a) and (b) that increasing  $T$  leads to larger energy splitting of JRMs. In this scenario, it can be clearly noticed from Figs. 3(c) and (d) that the overlap of exponentially decaying tails in the intermediate region gives rise to strong quantum tunneling for decreasing DW separation. Consequently, one can witness the existence of strong hybridized JRMs.

We should mention here that the nature of the quantum tunneling and hybridized states depends not only on  $\Delta_0$  and  $D_s$  but also has a dependency on the DW width  $\xi$  (since  $\Delta E \propto e^{-c\xi}$  as discussed in the Appendix B1). One may notice from Fig. 4(c) that a sharp DW results in strong tunneling and energy splitting of JRMs, whereas tunneling and splitting go to zero for a large DW width.

## B. Numerical Study

We begin by presenting the energy spectra in real space. We obtain real-space energy spectra by diago-

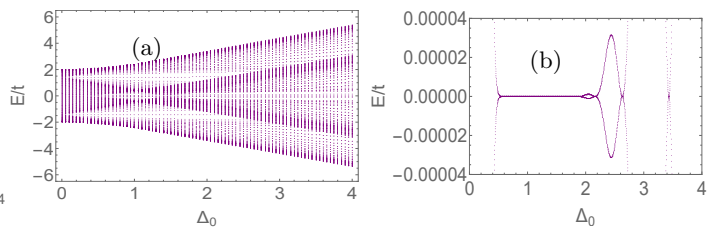


FIG. 5. (a) **Real-space energy spectra** as a function of domain wall amplitude  $\Delta_0$  under OBC. (b) The corresponding **low-energy spectra**. Here, we set  $L = 256$ ,  $\xi/a = 10$  and  $i_0 = L/2$ .

nalizing Eq. (1) for  $\theta = \pi/2$  with the periodic hopping modulation term now being replaced by  $\delta_{DW}$  (Eq. A2), and is plotted in Fig. 5. The figure clearly demonstrates the appearance of additional in-gap modes, including two nonzero energy in-gap modes. As we are interested in zero modes, we now focus on the low-energy spectra in Fig. 5(b), which shows the disappearance of ZES for very small and very large values of  $\Delta_0$ .

For  $0 < \Delta_0 < \sqrt{2}t$ , two in-gap states are exactly at zero energy and remain localized at the two ends of the chain[29]. This is because the hopping arrangements change at the chain center in such a way that no DW can exist at the chain center within this  $\Delta_0$  regime, similar to the no mass inversion and results in the non-existence of any DW for this  $\Delta_0$  regime as plotted in Fig. 2(b) (also notice the winding number plot Fig. 10(a) of Appendix B2). For  $\Delta_0 = \sqrt{2}t$ , the band gap closes, and the phase transition occurs. For  $\Delta_0 > \sqrt{2}t$ , the hopping arrangements changed within the lattice such that two DW created around the chain center. In this situation, zero-energy modes no longer exist; instead, we get near zero-energy states that exhibit a small energy splitting around  $E = 0$ . For  $\Delta_0 \gg \sqrt{2}t$ , more energy splitting is observed, making the result consistent with the analytical findings above.

Furthermore, with the help of the numerical method studied in the Appendix. A2, we plot the probability density of near zero-energy JRMs in Fig. 6. For the numerical results,  $\Delta_0 > \sqrt{2}t$  is chosen to ensure two mass inversions, thereby generating JRMs at both interfaces as studied analytically. The numerical plot reveals two hybridized ZES whose properties closely follow the analytical hybridized JR solution plotted in Fig. 3 and the probability density of these states illustrates a peak around the two mass-inversion interfaces, confirming their domain-wall origin. We also notice from the zoomed-in view of Fig. 6 that the JRMs, near the left interface, have a nonzero amplitude only at odd site index locations, while they have a nonzero amplitude only at even site index locations near the right interface. It clearly reflects that the JRMs have weight on A,C (B,D) sublattices near the left (right) interface. The numerical JRMs will also be strongly overlapped for  $\Delta_0 \gg \sqrt{2}t$ . This numerical prediction is consistent with the analytical findings discussed earlier.

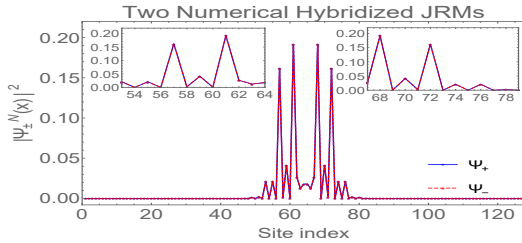


FIG. 6. **The numerical probability density of two JRMs.** The inset shows a zoomed-in view near two interfaces  $x_L$  and  $x_R$ , which depicts that the peak near the left interface appears only at odd site index positions, while near the right interface, it is visible only at even site index positions. We fix  $\Delta_0 = 2.5$ ,  $L = 128$ , and  $\xi/a = 10$ .

Based on the analytical and numerical study described above, we note here that, unlike the original SSH chain[28, 29], the JRMs are polarized in two sublattices in a way that no two consecutive sites have a nonzero amplitude of them. More explicitly, the finite amplitudes of the JRMs at the left interface are noticeable only on A,C sublattices, while they have a vanishing amplitude on B,D sublattices. This trend becomes opposite for the JRMs localized at the right interface.

Crucially, we might reasonably think of the pair of JR states bound to two interfaces as a quantum-mechanical double-well system. In quantum mechanics[40–43], considering a particle in a double-well potential with an infinite barrier width results in states individually peaked around the left well and the right well. While the finite barrier width allows tunneling of the states, due to which the wave functions begin to overlap and produce true eigenstates having symmetric and antisymmetric combinations[57].

Importantly, the existence of zero-energy JRMs in the present model cannot be understood simply in terms of an isolated unpaired lattice site, as in the case of a conventional SSH chain[28]. Instead, the JR zero modes originate from a spatial inversion of the effective Dirac mass  $M(x) = 2t^2 - \Delta^2(x)$ . For  $\Delta_0 > \sqrt{2}t$ , the mass profile generates two spatial locations where sign reversal occurs, thereby creating two interfaces between topologically distinct insulating phases. According to the JR mechanism, each mass inversion binds a localized zero-energy state[2]. Consequently, instead of a single, here a pair of exponentially localized JRMs emerge, one at each interface.

Although isolated (with no overlap) JRMs possess definite chirality ( $\Gamma_4|\Psi_L\rangle = +|\Psi_L\rangle$  and  $\Gamma_4|\Psi_R\rangle = -|\Psi_R\rangle$ ) and are pinned at zero energy, their finite overlap produces bonding and antibonding combinations with energies  $\pm T$ . These hybridized states are no longer the eigenstates of the chiral operator; rather, chiral symmetry exchanges the two states,  $\Gamma_4|\Psi_+\rangle = |\Psi_-\rangle$  and  $\Gamma_4|\Psi_-\rangle = |\Psi_+\rangle$ , while the Hamiltonian continues to satisfy the exact chiral symmetry  $\{\Gamma_4, \mathcal{H}_k\} = 0$ . Consequently, the energy splitting does not indicate chiral-symmetry breaking but instead arises from the finite

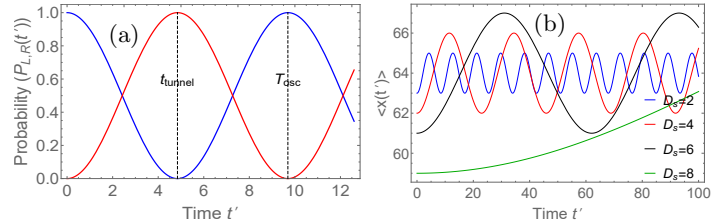


FIG. 7. (a) **Probability amplitude** as a function of time and (b) **time evolution of the position expectation value**  $\langle x(t') \rangle$ . In (a), the blue curve ( $P_L$ ) is the probability of finding the JRM at the left interface, while the red curve ( $P_R$ ) indicates the same at the right interface. For (a), we fix  $\Delta_0 = 12.5$ , and  $\xi/a = 10$ .

overlap of two topological interface modes. Since the JRMs are topologically protected, their topological invariant can also be estimated via change of winding number across each interface[68] (see Appendix B 2 for more details). It is worthwhile to note here that the topologically protected zero-energy modes trapped on a DW are a local property around a real-space defect, while the topological insulator is a property associated with the whole band and the entire Brillouin zone, not only the low effective description near the gap[69].

#### IV. COHERENT TUNNELING OSCILLATIONS

The study of coherent tunneling oscillations provides a direct dynamical probe of the hybridization between JR interface modes. Although the energy splitting of the near zero-energy JRMs reveals their overlap spectrally, the oscillatory transfer of probability density between the interfaces offers a real-time manifestation of this hybridization. Following [40–43], we begin by considering the JRMs initially prepared at the left interface  $|\Psi(x, 0)\rangle = |\Psi_L(x)\rangle$  (notice Eq. (9)) with  $|\Psi_L(x)\rangle = \frac{|\Psi_+(x)\rangle + |\Psi_-(x)\rangle}{\sqrt{2}}$ . Time evolution gives

$$|\Psi(x, t')\rangle = \frac{e^{-iE_+t'}|\Psi_+(x)\rangle + e^{-iE_-t'}|\Psi_-(x)\rangle}{\sqrt{2}}, \quad (12)$$

After rewriting it on a localized basis, one readily finds the evolution of the state as

$$|\Psi(x, t')\rangle = \cos(Tt')|\Psi_L(x)\rangle - i \sin(Tt')|\Psi_R(x)\rangle, \quad (13)$$

from which we now acquire the probability amplitudes between the two interfaces as

$$\left. \begin{aligned} P_L(t') &= |\langle \Psi_L(x) | \Psi(x, t') \rangle| = \cos^2(Tt') \\ P_R(t') &= |\langle \Psi_R(x) | \Psi(x, t') \rangle| = \sin^2(Tt') \end{aligned} \right\} \quad (14)$$

where  $T = \Delta T_0 e^{-c\xi}$  (or  $T = \Delta T_0 e^{-\kappa D_s}$ , for details, see Appendix B 1) denotes the actual tunneling matrix element between the two JRMs, with  $D_s = \frac{2\xi}{a} \operatorname{arctanh}\left(\frac{\sqrt{2}t}{\Delta_0}\right)$ . Thus, at  $t' = 0$ , the JRMs are entirely localized at the left interface. Then, they tunnel to

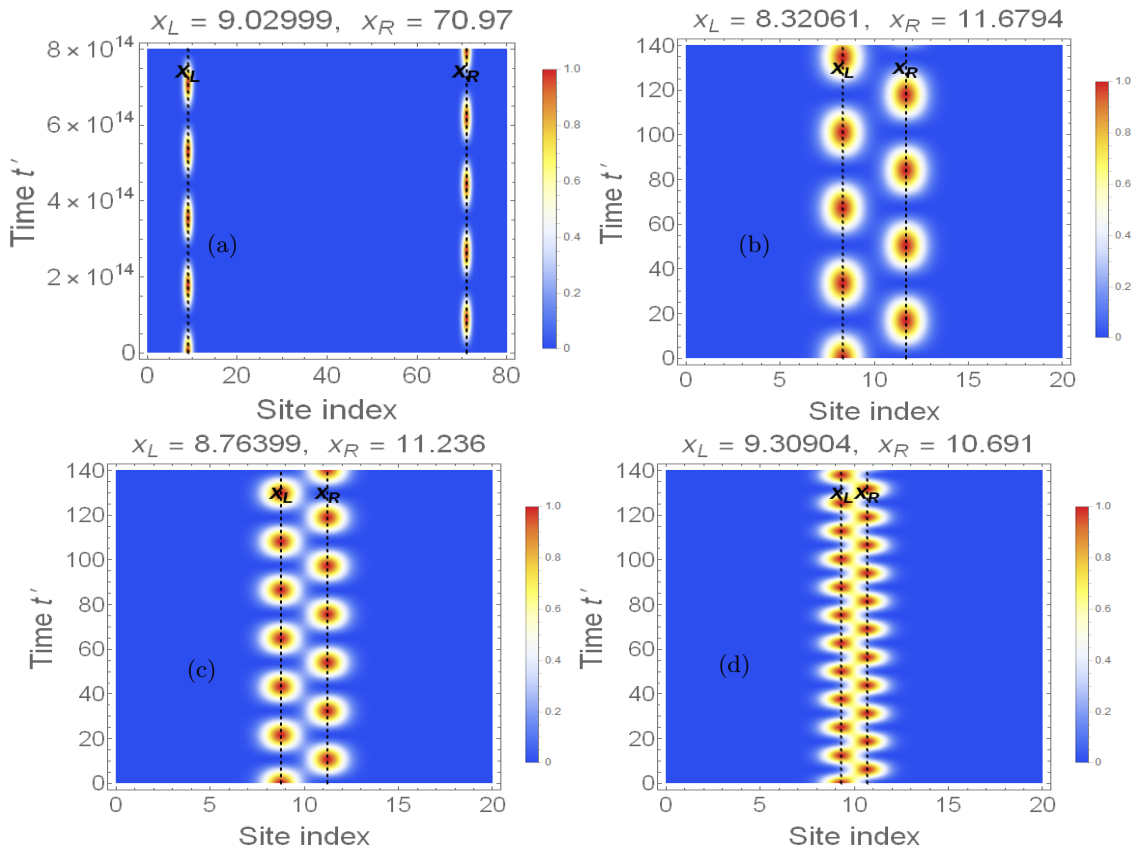


FIG. 8. **Probability density  $\rho(x, t')$  illustrating coherent tunneling between two JRMs localized at the interfaces  $x_L$  and  $x_R$  for varying  $\Delta_0$  and fixed  $\xi = 10$ .** The vertical dashed lines mark the interface positions  $x_L$  and  $x_R$ . Other parameters are: (a)  $L = 80$ ,  $\Delta_0 = 1.42$ , (b)  $L = 20$ ,  $\Delta_0 = 8.5$ , (c)  $L = 20$ ,  $\Delta_0 = 11.5$ , and (d)  $L = 20$ ,  $\Delta_0 = 20.5$ .

the right interface with tunneling time  $t' = t_{\text{tunnel}} = \frac{\pi}{2T}$  and periodically back to the left interface with a full oscillation period given by  $t' = T_{\text{osc}} = \frac{\pi}{T} = \frac{2\pi}{\Delta E}$ . This periodic behavior provides a direct dynamical manifestation of topological quantum tunneling in the modified SSH chain, exactly like a Rabi oscillation in a two-level quantum-mechanical double-well system[43, 57, 58]. To demonstrate the nature of dynamical tunneling oscillations between the JRMs, we plot Eq. (14) for  $\Delta_0 = 12.5$  and  $\xi/a = 10$  in Fig. 7(a). For the chosen set of parameter values, the system exhibits  $t_{\text{tunnel}} \approx 4.845$  and  $T_{\text{osc}} \approx 9.691$ , which are correctly marked by dashed vertical lines. We also notice that  $P_L(t')$  and  $P_R(t')$  are out of phase and the total probability density is conserved  $P_L(t') + P_R(t') = 1$ . We can witness slower oscillations for  $\Delta_0 = \sqrt{2}t^+$ . On the other hand, one can also look at the expectation value,  $\langle x(t') \rangle = x_0 - \frac{D_s}{2} \cos(2Tt')$ , the characteristic curve plotted in Fig. 7(b), which measures the average position of the probability density of JRMs at time  $t'$ . The oscillatory nature of  $\langle x(t') \rangle$  between  $x_L$  and  $x_R$  is a direct signature of coherent tunneling and oscillations becoming almost frozen for large  $D_s$ , as expected[70].

To shed light on the coherent tunneling oscillations more clearly, we can now investigate the density func-

tion  $\rho(x, t') = |\Psi(x, t')|^2 = \rho_{AC}(x, t') + \rho_{BD}(x, t')$  (with  $\rho_{AC}(x, t') = \cos^2(Tt')\Psi_L^2(x)$  and  $\rho_{BD}(x, t') = \cos^2(Tt')\Psi_R^2(x)$ ) for varying  $\Delta_0$  but with fixed  $\xi$  and is presented in Fig. 8. The density plot suggests that the density remains confined exactly at the two interfaces, confirming that the JRMs are topological interface modes rather than bulk excitations. In all plots, the periodic alteration of dense spots is a hallmark of coherent tunneling oscillations between two JRMs. Moreover, this figure clearly illustrates the gradual evolution from independent JRMs to strongly hybridized JRMs as the interface separation is progressively reduced. We notice from Fig. 8(a) that the tunneling period,  $T_{\text{osc}}$ , associated with the density transfer between the left and right JRMs becomes extremely high for exceedingly large interface separations, indicating negligible density transfer between the modes. This is the regime where  $D_s \gg l$  and overlap  $\langle \Psi_L | \Psi_R \rangle \approx 0$ . As a result, almost static vertical stripes localized at  $x_L$  and  $x_R$  demonstrate the decoupled JRMs. The tunneling period decreases when interface separation decreases, reflecting that the density transfer between the JR modes becomes faster, as can be seen from Figs. 8(b), (c) and (d). Nevertheless, this behavior again indicates that the decreasing interface separation markedly enhances the overlap between

the JRMs, thereby strengthening the tunneling and giving rise to pronounced coherent tunneling oscillations. In particular, notice Fig. 8(c) where oscillation frequency increases substantially, and density transfer occurs more rapidly. However, in Fig. 8(d), the density spot almost merges and undergoes very rapid oscillations such that the distinction between the JRMs at the left and right interfaces becomes less pronounced. This corresponds to strong hybridization, in agreement with our earlier observations. A similar tunneling behavior can be found in a quantum mechanical double-well system[58]. As is intuitively obvious, the tunneling period shows an increasing tendency (exponential nature) with increasing DW separation as well as increasing DW width  $\xi$  and is plotted in Fig. 11 (see Appendix B3). As the tunneling period is governed by the overlap of the exponentially localized JR wavefunctions, it therefore encodes information about the localization length and overlap of the JR wavefunctions. Interestingly, we can observe the same tunneling oscillations for varying  $\xi$  (while  $\Delta_0$  has to be fixed) as shown in Fig. 12 of Appendix B3.

In order to realize the change in sublattice character during tunneling, we need to study sublattice polarization density  $m(x, t) = \rho_{AC}(x, t) - \rho_{BD}(x, t)$ , which plays the role of magnetization or pseudospin density[18, 21, 71–73]. Thus,  $m(x, t)$  in Fig. 9(a) not only shows tunneling between JRMs but also depicts their sublattice polarization near each interface. At  $t' = 0$ ,  $m(x, 0) > 0$  ( $\rho_{AC}(x, t') > \rho_{BD}(x, t')$ ) indicates that the JRMs at the left interface are entirely (A,C) sublattice polarized. At  $t_{\text{tunnel}} \approx 8.16$ ,  $m(x, t_{\text{tunnel}}) < 0$  ( $\rho_{BD}(x, t') > \rho_{AC}(x, t')$ ) reflects that JRMs at the right interface are (B,D) sublattice polarized. After a full oscillation period  $T_{\text{osc}} \approx 16.32$ , the JRMs return to the initial configuration. The red and blue dashed horizontal lines in Fig. 9(a) correctly mark these characteristic times. Furthermore, for the oscillatory center  $x_C(t')$ , we get the polarization density as  $m(x, t') = \sqrt{\alpha/\pi} \cos(2Tt') e^{-\alpha(x-x_C(t'))^2}$  such that  $x_C(t')$  oscillates between the two interfaces, mimicking the motion of the expectation value  $\langle x(t') \rangle$  (discussed before). Figs. 9(a) and (b) clearly illustrate the periodic exchange of both localization and sublattice polarization of hybridized JRMs between the two interfaces: forces to consider the pair of oscillatory JRMs as a “*Jackiw-Rebbi molecule*”, analogous to tunneling in coupled quantum dots and hybridization of Majorana zero modes in topological superconductors[35, 36, 39]. Further, such behavior provides a topological realization of molecular bonding and antibonding orbitals[42, 59] through the hybridization of JRMs bound to the DW.

It is noteworthy to note here that, since the JRMs belong to different sublattice sectors, the oscillations are not only spatial but also involve the periodic transfer of sublattice polarization between two interfaces. This makes the dynamics richer than that of a simple Schrödinger double-well system[43, 57, 58].

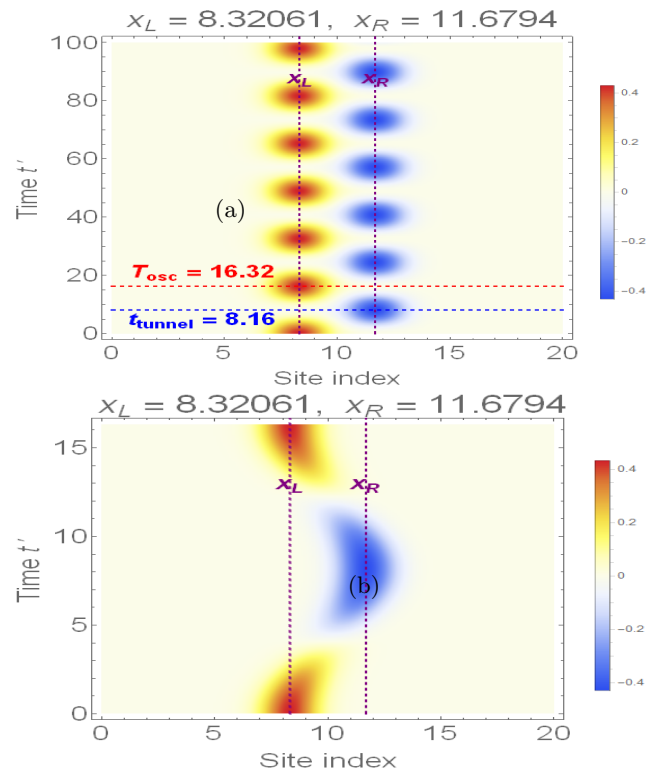


FIG. 9. (a) **Sublattice polarization based oscillations between JRMs** and (b) **spatio-temporal evolution of polarization density  $m(x, t')$** . The vertical dashed lines mark the interface positions  $x_L$  and  $x_R$ . In both plots, red/yellow ( $m > 0$ ) in the color bar represents that JRMs at the left interface have weight only on (A,C) sublattices, whereas blue ( $m < 0$ ) dictates that JRMs at the right interface predominantly occupy the (B,D) sublattices and equal occupation of the two sectors is marked by white ( $m \simeq 0$ ) color. Here, we set  $\Delta_0 = 8.5$ , and  $\xi/a = 10$ .

## V. SUMMARY AND CONCLUSIONS

To summarize, in this article, we have investigated the formation, hybridization, and coherent tunneling dynamics of zero-energy JRMs in a modified SSH chain. Employing an analytical continuum description around the quadratic point  $k = 0$  does not produce a topologically protected JRM as the effective Dirac mass  $M(x) = -\Delta^2(x)$  does not undergo a topological sign inversion under the kink profile and the result is consistent with the previous study[29]. Interestingly, employing a continuum description around the Dirac-type points  $k = \pm\pi/4$ , we showed that the low-energy excitations are governed by an effective Dirac Hamiltonian with a position-dependent mass term,  $M(x) = 2t^2 - \Delta^2(x)$ , where  $\Delta(x)$  assumes a kink-type domain-wall profile like that shown in Eq. (A1). Unlike the conventional SSH model[28], here the effective Dirac mass  $M(x)$  shows double sign reversal around the chain center  $x_0$  (specifically at  $x_{L,R} = x_0 \pm \frac{\xi}{a} \operatorname{arctanh}\left(\frac{\sqrt{2}t}{\Delta_0}\right)$ ) when the DW

amplitude exceeds the critical value ( $\Delta_0 > \sqrt{2}t$ ). Consequently, two spatially separated topological interfaces emerge, each supporting a localized JR bound state.

The appearance of individual zero-energy JRMs and near zero-energy hybridized JRMs at the interfaces is entirely determined by the interface separation  $D_s = \frac{2\xi}{a} \operatorname{arctanh}(\frac{\sqrt{2}t}{\Delta_0})$ . Using both analytical (effective two-state description) and numerical (diagonalization of real-space Hamiltonian) calculations, we demonstrate that the two exact zero-energy JRMs are infinitely far apart when the interface separation is infinite. For finite interface separation, the overlap of their exponentially decaying tails produces a finite quantum tunneling that lifts the exact zero-energy degeneracy and generates symmetric and antisymmetric combinations of JRMs separated by finite energy splitting  $\Delta E$ , which are identical to the bonding-antibonding states in a double-well quantum system[40–43]. The corresponding energy splitting decreases exponentially with increasing interface separation (typically scaled as  $\Delta E \propto e^{-\kappa D_s}$  with  $\kappa^{-1}$  giving the JR localization length) and with increasing interface width (typically scaled as  $\Delta E \propto e^{-\epsilon\xi}$ ).

To elucidate the coherent tunneling dynamics of hybridized JRMs, we analyzed the real-time evolution of JRMs initially localized at the left interface. The dynamics is governed by tunnel splitting  $\Delta E$  and the corresponding occupation probabilities oscillate as  $P_L(t') = \cos^2(Tt')$  and  $P_R(t') = \sin^2(Tt')$ , demonstrating that the JRMs initially localized at the left interface undergo coherent quantum tunneling to the right interface with tunneling time  $t_{\text{tunnel}}$  and return periodically to the left interface with full oscillation period  $T_{\text{osc}}$ . However, looking at the average position  $\langle x(t') \rangle$  of the probability density of JRMs at time  $t'$ , we notice the oscillatory nature of it between  $x_L$  and  $x_R$ , which is a hallmark of coherent tunneling oscillations. This behavior constitutes a topological realization of Rabi oscillations in a quantum mechanical double-well system[43, 57, 58] and provides a direct manifestation of quantum coherence between spatially separated defect states (JRMs). The resulting dynamics is formally equivalent to those of a quantum particle in a double-well potential[43, 57, 58]. Moreover, the density function  $\rho(x, t') = \rho_{AC}(x, t) + \rho_{BD}(x, t)$  nicely portrays the evolution from independent JRMs (with high  $T_{\text{osc}}$ ) to strongly hybridized JRMs (with low  $T_{\text{osc}}$ ) with the decrease of interface separation.

To visualize sublattice polarization during the tunneling process, we introduce the sublattice polarization density,  $m(x, t') = \rho_{AC}(x, t) - \rho_{BD}(x, t)$ , which acts as a local pseudospin polarization density in the effective (AC,BD) sublattice basis[18, 21, 71–73]. The spatiotemporal evolution of  $m(x, t')$  directly visualizes the coherent exchange of both localization and sublattice character of hybridized JRMs between the two interfaces, providing a real-space signature of coherent tunneling and hybridization. Thus, the periodic exchange of localization, sublattice polarization, and probability density establishing the hybridized JRMs pair as a topological analogue of

a diatomic molecular system, which may be viewed as a “*Jackiw–Rebbi molecule*”.

Our results establish a unified connection between topological defect states, quantum tunneling, and molecular-state formation in 1D topological systems. The modified SSH chain, therefore, provides a controllable platform for studying the coherent dynamics of topological bound states, where the localization length, interface separation, and tunnel coupling can be tuned through the domain-wall parameters. Beyond the tunneling phenomena discussed here, the effective mass profile naturally creates a finite topological cavity bounded by two mass-inversion points, suggesting possible connections to resonant cavity modes, quasi-bound states, and analogue horizon physics[74–78]. Moreover, understanding the hybridization of spatially separated JRMs is therefore crucial for designing the topological quantum devices[79, 80], where controlled coupling between JRMs serves as a key resource.

The present work opens several promising directions for future research, including Floquet engineering of topological states and defect modes [81–84], disorder-induced modifications of topological bound states and coherent dynamics [85, 86], interaction effects in topological zero-mode systems [87], non-Hermitian extensions of topological interface physics [88–90], and many-body realizations in synthetic quantum platforms [91–94]. More broadly, the demonstrated interplay between topology, localization, and quantum tunneling highlights the potential of engineered domain-wall structures as versatile building blocks for topological quantum-state manipulation and transport[22, 38]. Moreover, the result of the paper is interesting and plausible in connection to experiments on quantum dot SSH models[95, 96]. Furthermore, our predictions of tunnel splitting and coherent oscillations of JRMs should be experimentally accessible in several synthetic topological platforms, particularly in femtosecond-laser-written photonic waveguide arrays[97, 98], cold-atom realization of SSH chains[31, 92, 99], graphene-based engineered Dirac systems[100], topological photonic or acoustic lattices[101] and quantum gas microscopy[102]. In all such systems, the spatially varying hopping amplitudes can be engineered with high precision. Specifically, in photonic systems, the propagation distance acts as an effective time coordinate, allowing direct observation of coherent oscillations of light intensity between the two interface modes, while quantum gas microscopy enables site-resolved imaging of analogous tunneling dynamics in cold-atom lattices. These platforms provide a realistic route for observing the predicted hybridization, coherent tunneling, and sublattice-polarization dynamics of JR zero modes. Lastly, we should mention here that in the future, we have a plan to study the out-of-equilibrium behavior of such a modified SSH model, subjected to a quantum quench that leads to an effective metal-insulator transition for the conventional SSH model[103].

## ACKNOWLEDGEMENTS

The author thanks S. Kar and S. Mandal (IOP, Bhubaneswar) for the fruitful discussions. The author acknowledges financial support from DST-SERB (ANRF), Government of India under grant no. CRG/2022/002781.

## Appendix A

### 1. Analytical Jackiw-Rebbi Method: Continuum limit of Momentum-space Hamiltonian

In the seminal work by JR[1], one-dimensional Dirac fermions are coupled with a solitonic field. The solitonic field was introduced in the low-energy effective Dirac Hamiltonian as a position-dependent mass term, the specific structure of which determines the topology of the system. A change of sign in the mass term about the DW yields localized ZES at its position. In this respect, it is ludicrous to mention that intermediate-order topological interfacial states can be found in a  $n$ -dimensional SSH model as elaborated in Ref.[104]. The topological defect of the solitonic field is known as a kink. Polyacetylene is the condensed-matter realization of such a situation at any domain wall junction between two possible dimerizations ( $\Delta/t < 0$  and  $\Delta/t > 0$ )[18, 19]. The general recipe for the JR method is as follows:

Expand the Bloch Hamiltonian Eq. (2) around the gap closing point such that the low-energy Hamiltonian follows a 1D Dirac equation where the mass term becomes position-dependent (spatially inhomogeneous), then change its sign by introducing a topological defect. The typical choice of mass profile, centered at site  $x = x_0$ , is defined as

$$M(x) = M_0 \tanh \left[ \frac{x - x_0}{\xi/a} \right], \quad (\text{A1})$$

in which  $M_0$ ,  $\xi$  and  $a$  denote the amplitude of the mass profile, the width of the mass profile and the lattice spacing, respectively. Now,  $M(x)$  should satisfy  $\lim_{x-x_0 \rightarrow -\infty} M(x) = -M_0$  and  $\lim_{x-x_0 \rightarrow \infty} M(x) = M_0$ . For  $M_0 > 0$ , two constant fields  $\pm M_0$  represent the two different phases for our system, and only topological texture holds a single localized state with energy  $E = 0$ [18, 19, 69]. To describe the zero-energy JR mode, we allow the kink-shaped mass profile  $M(x)$  to interpolate between  $M_0$  and  $-M_0$  and create a DW at  $x = x_0$ [2]. Using this mechanism, one can analytically investigate the JR zero modes in the presence of DWs.

### 2. Real-space Analysis: Numerical Lattice Study

To simulate the JR mode numerically, we need to construct the hopping position dependent such that they flip their relative magnitudes across the center of DW.

Following[29, 30], we begin by introducing a single domain wall for our model in real-space, with the modulation in hopping strength now taking the following form

$$\delta_{DW} = \delta_{i,0} \tanh \left[ \frac{i - i_0}{\xi/a} \right] = \Delta_0 \tanh \left[ \frac{i - i_0}{\xi/a} \right] \cos[(i-1)\theta], \quad (\text{A2})$$

in which  $\Delta_0$ ,  $\xi$ , and  $a$  represent, respectively, the amplitude of DW, the width of DW, and the lattice spacing. Here, the index  $i$  refers to the location of the  $i$ -th site, and the parameter  $i_0$  fixes the position of the DW. In this study, we fix the position of the DW at  $i_0 = L/2$  in a way that the left side ( $i < i_0$ ) is in one topological phase and the right side ( $i > i_0$ ) lies in another topological phase. A smooth (sharp) DW can be achieved for large (small)  $\xi$ . With this, the diagonalization of the Hamiltonian given in Eq. (1) under OBC results in two zero modes.

We should emphasize here that, unlike the physical edge of the chain, this type of DW creates an effective or artificial boundary inside the chain, separating and connecting two distinct topological phases of the system. It is noted that one may consider the physical boundaries or edges of the SSH chain as DWs with the vacuum or surrounding and the DWs, similar to the physical edge of the SSH chain, host zero-energy localized states[29].

### 3. Block off-diagonal form of Eq. (2)

Now, the Bloch Hamiltonian Eq. (2) can be changed to be block off-diagonal form as it has the chiral symmetry[29]. We first apply the unitary transformation with the unitary matrix

$$U = \begin{pmatrix} 1 & 0 & 0 & 0 \\ 0 & 0 & 1 & 0 \\ 0 & 1 & 0 & 0 \\ 0 & 0 & 0 & 1 \end{pmatrix} \quad (\text{A3})$$

makes the Hamiltonian  $\mathcal{H}(k)$  in Eq. (2) into the block off-diagonal form  $\mathcal{H}(k) \rightarrow U\mathcal{H}(k)U^{-1} = \begin{pmatrix} 0 & V \\ V^\dagger & 0 \end{pmatrix}$ , where the upper off-diagonal block reads

$$V(k) = \begin{pmatrix} (t + \Delta) & te^{-4ik} \\ t & (t - \Delta) \end{pmatrix} \quad (\text{A4})$$

with  $\text{Det}[V(k)] = (t^2 - \Delta^2) - t^2 e^{-4ik}$ . Thus,  $h_x(k) = \text{Re}[\text{Det}[V(k)]] = (t^2 - \Delta^2) - t^2 \cos k$  and  $h_y(k) = \text{Im}[\text{Det}[V(k)]] = -t^2 \sin k$ . Thus, we can write Eq. (2) as follows:

$$\mathcal{H}(k) = h_x(k)\sigma_x + h_y(k)\sigma_y \quad (\text{A5})$$

## Appendix B

### 1. Asymptotic form of $T$ and $\Delta E$

As we know,  $T \propto e^{-\frac{\alpha D_s^2}{4}}$  and  $\Delta E \propto 2e^{-\frac{\alpha D_s^2}{4}}$ . Although the overlap formula originally looked Gaussian in  $D_s$ , we

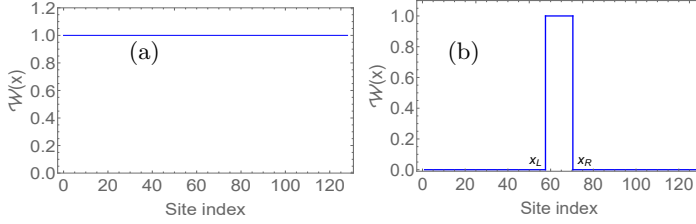


FIG. 10. **Winding number** for (a)  $\Delta_0 < \sqrt{2}t$  and (b)  $\Delta_0 < \sqrt{2}t$ . Here, we set  $L = 128$ ,  $\xi/a = 10$ .

now convert it into an asymptotic form (as for large  $D_s$ , the tunnel splitting is governed by the far tails, not the local Gaussian core). Substituting  $\alpha = \frac{2\sqrt{2}t(\Delta_0^2 - 2t^2)}{v\Delta_0\xi}$  and  $D_s = \frac{2\xi}{a} \operatorname{arctanh}\left(\frac{\sqrt{2}t}{\Delta_0}\right)$ , we get  $\Delta E = 2\Delta E_0 e^{-c\xi}$  with  $c = \frac{\sqrt{2}t(\Delta_0^2 - 2t^2)}{2va\Delta_0} \left[2 \operatorname{arctanh}\left(\frac{\sqrt{2}t}{\Delta_0}\right)\right]^2$  and  $l_\xi = c^{-1}$  is not the physical localization length as it merely characterizes how rapidly the tunnel splitting decreases when the domain-wall width  $\xi$  is varied.

Now, substituting  $\xi = \frac{D_s}{\frac{2}{a} \operatorname{arctanh}\left(\frac{\sqrt{2}t}{\Delta_0}\right)}$  into  $\alpha$ , one obtains  $\Delta E = 2\Delta E_0 e^{-\kappa D_s}$  with  $\kappa = \frac{2\sqrt{2}t(\Delta_0^2 - 2t^2)}{v\Delta_0} \left[\frac{2}{a} \operatorname{arctanh}\left(\frac{\sqrt{2}t}{\Delta_0}\right)\right]$  and  $l_D = \kappa^{-1}$  representing the physical localization length as the JRMs far from the interface behave as  $\Psi_{L,R}(x) \sim e^{-\kappa|x-x_{L,R}|}$ .

## 2. Bulk Winding Number Calculation

For the domain-wall configuration, the local (as translational invariance is broken, so the winding number is not globally defined) winding number can be calculated by  $\mathcal{W}(x) = \frac{1}{2\pi} \int_{BZ} dk \partial_k \arg(h_x(k, x) + ih_y(k, x))$  with  $h_x(k, x) = t^2 - \Delta^2(x) - t^2 \cos 4k$  and  $h_y(k, x) = -t^2 \sin 4k$ . Then, one can attain

$$\mathcal{W}(x) = \begin{cases} 1, & 0 < |\Delta(x)| < \sqrt{2}t \\ 0, & |\Delta(x)| > \sqrt{2}t \end{cases} \quad (\text{B1})$$

**Case I:** for  $\Delta_0 < \sqrt{2}t$ ,  $0 < |\Delta(x)| < \Delta_0 < \sqrt{2}t$ , and no mass inversion is noticeable. So  $\mathcal{W}(x) = 1 \forall x$  (see Fig. 10(a)) and non-existence of JR modes.

**Case II:** For  $\Delta_0 > \sqrt{2}t$ , the condition  $M(x) = 0$  give mass inversion at the two interfaces at  $x_L = x_0 - x_*$  and  $x_R = x_0 + x_*$ . Inside the two interfaces  $x_L < x < x_R$ , the condition  $|\Delta(x)| < \sqrt{2}t$  giving  $\mathcal{W}(x) = 1$ . While outside the region,  $|\Delta(x)| > \sqrt{2}t$  condition provide  $\mathcal{W}(x) = 0$  (look at the Fig. 10(b)). Thus, we arrive at

$$\mathcal{W}(x) = \begin{cases} 0, & x < x_L \\ 1, & x_L < x < x_R \\ 0, & x > x_R \end{cases} \quad (\text{B2})$$

Therefore, at  $x_L$ ,  $\Delta\mathcal{W}(x_L) = +1$ , while  $\Delta\mathcal{W}(x_R) = -1$  at  $x_R$ . Similar to bulk-boundary correspondence, here the bulk-defect correspondence provides  $N(x_L) = |\Delta\mathcal{W}(x_L)| = 1$  and  $N(x_R) = |\Delta\mathcal{W}(x_R)| = 1$ . Thus, each interface supports a JR mode. Hence, the interface states exemplify bulk-defect correspondence, where the change in the bulk winding number across the domain wall guarantees localized JRMs[68].

## 3. Graph For Tunneling Time and Probability Density

As we know  $T_{osc} = \frac{\pi}{T} = \frac{2\pi}{\Delta E}$ , therefore, from Appendix B1, we attain  $T_{osc} = \frac{\pi}{\Delta E_0} e^{c\xi}$  and  $T_{osc} = \frac{\pi}{\Delta E_0} e^{\kappa D_s}$ . The nature of the tunneling period with  $D_s$  and  $\xi$  is plotted in Fig. 11, which shows the exponential growth of  $T_{osc}$  with  $D_s$  and  $\xi$ .

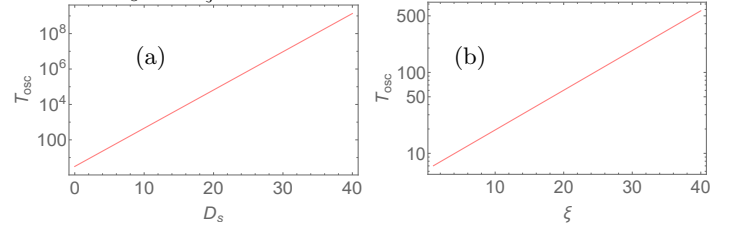


FIG. 11. **Tunneling period (log scale)** vs interface separation  $D_s$  (a) and vs interface width  $\xi$  (b). For the plot, we consider  $\Delta_0 = 12.5$ .

In Fig. 12, we depict the probability density function for different  $\xi$ , keeping  $\Delta_0$  fixed. The plot illustrates that density transfer becomes progressively slower as  $\xi$  increases (see (Fig. 12(a))). One can notice the strong hybridization for a very sharp domain wall (Fig. 12(d)). The linear correspondence between  $D_s$  and  $\xi$  is expected as  $D \propto \xi$ .

- [1] R. Jackiw and C. Rebbi, Solitons with Fermion number  $\frac{1}{2}$ , *Phys. Rev. D* **13**, 3398 (1976).
- [2] R. Jackiw, Fractional and Majorana fermions: the physics of zero-energy modes, *Physica Scripta* **2012**, 014005 (2012).
- [3] R. Jackiw and J. Schrieffer, Solitons with fermion number  $\frac{1}{2}$  in condensed matter and relativistic field theories,

*Nucl. Phys. B* **190**, 253 (1981).

- [4] J. Goldstone and F. Wilczek, Fractional quantum numbers on solitons, *Phys. Rev. Lett.* **47**, 986 (1981).
- [5] R. Jackiw, A. Kerman, I. Klebanov, and G. Semenoff, Fluctuations of fractional charge in soliton anti-soliton systems, *Nucl. Phys. B* **225**, 233 (1983).
- [6] C. Nayak, S. H. Simon, A. Stern, M. Freedman, and S.

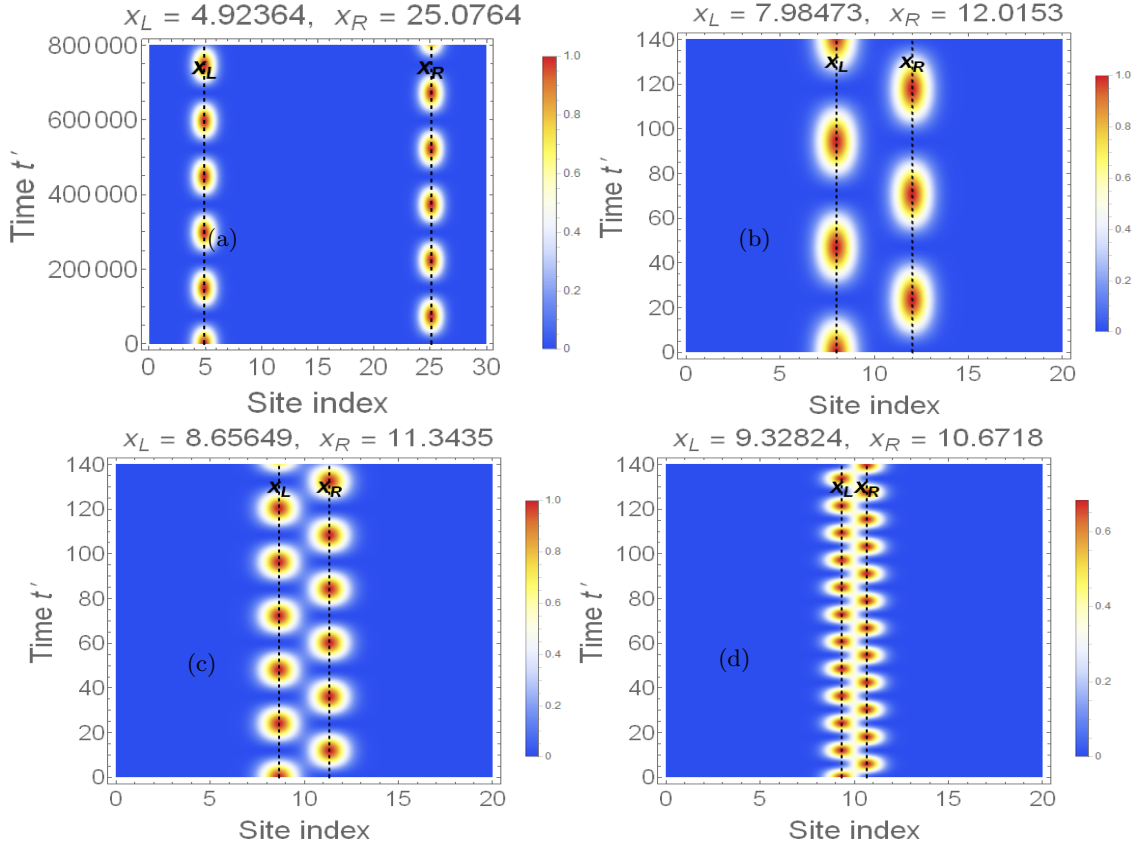


FIG. 12. Probability density  $\rho(x, t)$  illustrating coherent tunneling between two JR modes localized at the interfaces  $x_L$  and  $x_R$  for varying  $\xi$  and fixed  $\Delta_0 = 8.5$ . The vertical dashed lines indicates the interface positions  $x_L$  and  $x_R$ . Other parameters are: (a)  $L = 30$ ,  $\xi/a = 60$ , (b)  $L = 20$ ,  $\xi/a = 12$ , (c)  $L = 20$ ,  $\xi/a = 8$ , and (d)  $L = 20$ ,  $\xi/a = 4$ .

- Das Sarma, Non-Abelian anyons and topological quantum computation, *Rev. Mod. Phys.* **80**, 1083 (2008).
- [7] A. J. Heeger, Nobel Lecture: Semiconducting and metallic polymers: The fourth generation of polymeric materials, *Rev. Mod. Phys.* **73**, 681 (2001).
- [8] A. J. Heeger, S. Kivelson, J. R. Schrieffer, and W. P. Su, Solitons in conducting polymers, *Rev. Mod. Phys.* **60**, 781 (1988).
- [9] M. Z. Hasan and C. L. Kane, Colloquium: Topological insulators, *Rev. Mod. Phys.* **82**, 3045 (2010).
- [10] X.-L. Qi and S.-C. Zhang, Topological insulators and superconductors, *Rev. Mod. Phys.* **83**, 1057 (2011).
- [11] L. Lu, J. D. Joannopoulos, and M. Soljačić, Topological photonics, *Nature Photon* **8**, 821–829 (2014).
- [12] T. Ozawa et. al., Topological photonics, *Rev. Mod. Phys.* **91**, 015006 (2019).
- [13] J. W. You, Q. Ma, Z. Lan, Q. Xiao, N. C. Panoiu, and T. J. Cui, Reprogrammable plasmonic topological insulators with ultrafast control, *Nat. Commun.* **12**, 5468 (2021).
- [14] Z. Xu, X. Kong, J. Chang, D. F. Sievenpiper, and T. J. Cui, Topological Flat Bands in Self-Complementary Plasmonic Metasurfaces, *Phys. Rev. Lett.* **129**, 253001 (2022).
- [15] X. Ni, S. Yves, A. Krasnok, and A. Alu, Topological metamaterials, [arXiv:2211.10006](https://arxiv.org/abs/2211.10006) [physics.optics] (2022).
- [16] W. Zhu et. al., Topological phononic metamaterials, *Rep. Prog. Phys.* **86** 106501 (2023).
- [17] S. Jana, A. Saha, and S. Das, Jackiw-Rebbi zero modes in non-uniform topological insulator nanowire, *Phys. Rev. B* **100**, 085428 (2019).
- [18] W. P. Su, J. R. Schrieffer, and A. J. Heeger, Solitons in Polyacetylene, *Phys. Rev. Lett.* **42**, 1698 (1979).
- [19] W. P. Su, J. R. Schrieffer, and A. J. Heeger, Soliton excitations in polyacetylene, *Phys. Rev. B* **22**, 2099 (1980).
- [20] J. K. Asbóth, L. Oroszlány, and A. Pályi, “A Short Course on Topological Insulators”, Springer International Publishing, (2016).
- [21] S. Ryu and Y. Hatsugai, Topological Origin of Zero-Energy Edge States in Particle-Hole Symmetric Systems, *Phys. Rev. Lett.* **89**, 077002 (2002).
- [22] A. Y. Kitaev, Unpaired Majorana fermions in quantum wires, *Phys.-Usp.* **44** 131 (2001).
- [23] D. X. Horváth, S. Fraenkel, S. Scopu, and C. Rylands, Charge resolved entanglement in the presence of topological defects, *Phys. Rev. B* **108**, 165406 (2023).
- [24] F. M. D’Angelis, F. A. Pinheiro, D. Guery-Odelin, S. Longhi, and F. Impens, Fast and robust quantum state transfer in a topological Su-Schrieffer-Heeger chain with next-to-nearest-neighbor interactions, *Phys. Rev. Res.* **2**, 033475 (2020).
- [25] F. Munoz, F. Pinilla, J. Mella, and M. I. Molina, Topological properties of a bipartite lattice of domain wall

- states, *Sci. Rep.* **8**, 17330 (2018).
- [26] S. Longhi, Topological pumping of edge states via adiabatic passage, *Phys. Rev. B* **99**, 155150 (2019).
- [27] L. Qi, Y. Yan, Y. Xing, X. D. Zhao, S. Liu, W. X. Cui, X. Han, S. Zhang, and H. F. Wang, Topological router induced via long-range hopping in a Su-Schrieffer-Heeger chain, *Phys. Rev. Res.* **3**, 023037 (2021).
- [28] C.L. Kane, Chapter 1-Topological Band Theory and the  $\mathbb{Z}_2$  Invariant, *Contemporary Concepts of Condensed Matter Science*, Elsevier, Volume **6**, Pages 3-34 (2013).
- [29] S. Mandal, S. Kar, Topological solitons in a Su-Schrieffer-Heeger chain with periodic hopping modulation, domain wall, and disorder, *Phys. Rev. B* **109**, 195124 (2024).
- [30] M. Scollon and M. P. Kennett, Persistence of chirality in the Su-Schrieffer-Heeger model in the presence of on-site disorder, *Phys. Rev. B* **101**, 144204 (2020).
- [31] M. Atala, M. Aidelsburger, J. T. Barreiro, D. Abanin, T. Kitagawa, E. Demler, and I. Bloch, Direct measurement of the Zak phase in topological Bloch bands, *Nature Physics* **9**, 795–800 (2013).
- [32] S. Weimann, Topologically protected bound states in photonic parity–time-symmetric crystals, *Nature Materials* **16**, 433–438 (2017).
- [33] C. He, X.-C. Sun, X.-P. Liu, M.-H. Lu, Y. Chen, L. Feng, and Y.-F. Chen, Topological phononic states of underwater sound based on coupled ring resonators, *Applied Physics Letters* **108**, 031904 (2016).
- [34] C. L. Kane and T. C. Lubensky, Topological boundary modes in isostatic lattices, *Nature Physics* **10**, 39–45 (2014).
- [35] J. Alicea, New directions in the pursuit of Majorana fermions in solid state systems, *Rep. Prog. Phys.* **75**, 076501 (2012).
- [36] C. W. J. Beenakker, Search for Majorana Fermions in Superconductors, *Annual Review Condensed Matter Physics*. 4:113-136 (2013).
- [37] S. R. Elliott and M. Franz, Colloquium: Majorana fermions in nuclear, particle, and solid-state physics, *Rev. Mod. Phys.* **87**, 137 (2015).
- [38] Y. E. Kraus, Y. Lahini, Z. Ringel, M. Verbin, and O. Zeitlinger, Topological States and Adiabatic Pumping in Quasicrystals, *Phys. Rev. Lett.* **109**, 106402 (2012).
- [39] M. Bellec, U. Kuhl, G. Montambaux, and F. Mortessagne, Topological Transition of Dirac Points in a Microwave Experiment, *Phys. Rev. Lett.* **110**, 033902 (2013).
- [40] L. D. Landau and E. M. Lifshitz, *Quantum Mechanics: Non-Relativistic Theory*, 3rd ed. Pergamon Press, Oxford, 1977.
- [41] C. Cohen-Tannoudji, B. Diu, and F. Laloë, *Quantum Mechanics*, John Wiley & Sons, New York, 1977.
- [42] D. J. Griffiths and D. F. Schroeter, *Introduction to Quantum Mechanics*, 3rd ed. Chap. 8, Cambridge University Press, Cambridge, 2018.
- [43] R. Shankar, *Principles of Quantum Mechanics*, 2nd ed. New York: Springer, 1994.
- [44] A. J. Leggett, S. Chakravarty, A. T. Dorsey, M. P. A. Fisher, A. Garg, and W. Zwerger, Dynamics of the dissipative two-state system, *Reviews of Modern Physics* **59**, 1 (1987).
- [45] M. Grifoni, Dynamics of the dissipative two-state system under ac modulation of bias and coupling energy, *Physical Review E* **54**, R3086 (1996).
- [46] S. M. H. Halataei and A. J. Leggett, Tunnel splitting in asymmetric double well potentials: An improved wkb calculation (2017), [arXiv:1703.05758 \[quant-ph\]](https://arxiv.org/abs/1703.05758).
- [47] J. D. Swalen and J. A. Ibers, Potential Function for the Inversion of Ammonia Available to Purchase, *The Journal of Chemical Physics* **36**, 1914 (1962).
- [48] G. Burkard, D. Loss, and D. P. DiVincenzo, Coupled quantum dots as quantum gates, *Physical Review B* **59**, 2070 (1999).
- [49] M. Albiez, R. Gati, J. Fölling, S. Hunsmann, M. Cristiani, and M. K. Oberthaler, Direct Observation of Tunneling and Nonlinear Self-Trapping in a Single Bosonic Josephson Junction, *Physical Review Letters* **95**, 010402 (2005).
- [50] Y. Shin, G.-B. Jo, M. Saba, T. A. Pasquini, W. Ketterle, and D. E. Pritchard, Optical Weak Link between Two Spatially Separated Bose-Einstein Condensates, *Physical Review Letters* **95**, 170402 (2005).
- [51] T. Schumm, S. Hofferberth, L. M. Andersson, S. Wildermuth, S. Groth, I. Bar-Joseph, J. Schmiedmayer, and P. Krüger, Matter-wave interferometry in a double well on an atom chip, *Nature Physics* **1**, 57 (2005).
- [52] B. V. Hall, S. Whitlock, R. Anderson, P. Hannaford, and A. I. Sidorov, Condensate Splitting in an Asymmetric Double Well for Atom Chip Based Sensors, *Physical Review Letters* **98**, 030402 (2007).
- [53] M. H. Devoret, J. M. Martinis, and J. Clarke, Measurements of Macroscopic Quantum Tunneling out of the Zero-Voltage State of a Current-Biased Josephson Junction, *Physical Review Letters* **55**, 1908 (1985).
- [54] Y. Makhlin, G. Schön, and A. Shnirman, Quantum-State Engineering with Josephson-Junction Devices, *Reviews of Modern Physics* **73**, 357 (2001).
- [55] S. Levy, E. Lahoud, I. Shomroni, and J. Steinhauer, The a.c. and d.c. Josephson effects in a Bose-Einstein condensate, *Nature* **449**, 579 (2007).
- [56] J. Clarke and F. K. Wilhelm, Superconducting quantum bits, *Nature* **453**, 1031 (2008).
- [57] L. Zheng, G. Li, M.-S. Ding, Y.-L. Wang, and Y.-C. Zhang, Coherent wave packet dynamics in a double-well potential in a cavity, *International Journal of Modern Physics* **32**, 1850039 (2018).
- [58] R. Christie and J. Eastman, Quantum tunnelling and thermally driven transitions in a double-well potential at finite temperature, *J. Phys. A: Math. Theor.* **57**, 235005 (2024).
- [59] G. Grosso and G. Pastori Parravicini, *Solid State Physics*, Ch. 11 molecular bonding and double-well tunneling, 2nd ed. Academic Press, 2014.
- [60] S.Mandal, and S.Kar, Topology and PT Symmetry in a Non-Hermitian Su-Schrieffer-Heeger Chain with Periodic Hopping Modulation, *J. Phys.: Condens. Matter* **37**, 095602 (2025).
- [61] S. Kar, Edge state behavior in a Su-Schrieffer-Heeger like model with periodically modulated hopping, *J. Phys.: Condens. Matter* **36**, 065301 (9pp) (2024).
- [62] C.-K. Chiu, J. C. Y. Teo, A. P. Schnyder, and S. Ryu, Classification of topological quantum matter with symmetries, *Rev. Mod. Phys.* **88**, 035005 (2016).
- [63] A. Altland and M. R. Zirnbauer, Novel symmetry classes in mesoscopic normal-superconducting hybrid structures, *Phys.Rev.B* **55**, 1142 (1997).
- [64] V.Gurarie, Single particle Green’s functions and inter-

- acting topological insulators, *Phys. Rev. B* **83**, 085426 (2011).
- [65] Z. Wang and S. C. Zhang, Topological Invariants and Ground-State Wave functions of Topological Insulators on a Torus, *Phys. Rev. X* **4** 011006 (2014).
- [66] Y. He and C.-C. Chien, Non-Hermitian generalizations of extended Su–Schrieffer–Heeger models, *J. Phys.: Condens. Matter* **33** 085501 (2021).
- [67] M. McIntyre and G. Cairns, A new formula for winding number, In: *Geometriae Dedicata* **46.2**, pp. 149–159 (1993).
- [68] J. C. Y. Teo and C. L. Kane, Topological defects and gapless modes in insulators and superconductors, *Phys. Rev. B* **82**, 115120 (2010).
- [69] J. Cayssol, and J.-N. Fuchs, *J. Phys. Mater.* **4**, 034007 (2021).
- [70] The oscillation of  $\langle x(t') \rangle$  does not mean that a JR mode physically moves from one interface to the other. Instead, it means that the occupation probability tunnels back and forth between two fixed JR modes.
- [71] A. H. Castro Neto, F. Guinea, N. M. R. Peres, K. S. Novoselov, and A. K. Geim, *The electronic properties of graphene*, *Rev. Mod. Phys.* **81**, 109–162 (2009).
- [72] A. Altland, and B. Simons, *Condensed Matter Field Theory*, 2nd ed. Cambridge University Press, Cambridge, (2010).
- [73] M. I. Katsnelson, *Graphene: Carbon in Two Dimensions*, Cambridge University Press, Cambridge, (2012).
- [74] M. I. Katsnelson, K. S. Novoselov, and A. K. Geim, Chiral tunnelling and the Klein paradox in graphene, *Nat. Phys.* **2**, 620 (2006).
- [75] A. De Martino, L. Dell’Anna, and R. Egger, Magnetic confinement of massless Dirac fermions in graphene, *Phys. Rev. Lett.* **98**, 066802 (2007).
- [76] P. Recher and B. Trauzettel, Quantum dots and spin qubits in graphene, *Nanotechnology* **21**, 302001 (2010).
- [77] W. G. Unruh, Experimental Black-Hole Evaporation?, *Phys. Rev. Lett.* **46**, 1351 (1981).
- [78] C. Barceló, S. Liberati, and M. Visser, Analogue Gravity, *Living Rev. Relativity* **14**, 3 (2011).
- [79] K.-H. Jin et al., Topological quantum devices: a review, *Nanoscale* **15**, 11874–11902 (2023).
- [80] Y. Wang et al., Hybridization of Non-Hermitian Topological Interface Modes, *Newton* **2**, 100438 (2026).
- [81] V. Dal Lago, M. Atala, and L. E. F. Foa Torres, Floquet topological transitions in a driven one-dimensional topological insulator, *Phys. Rev. A* **92**, 023624 (2015).
- [82] T. Kitagawa, E. Berg, M. Rudner, and E. Demler, Topological characterization of periodically driven quantum systems, *Phys. Rev. B* **82**, 235114 (2010).
- [83] N. H. Lindner, G. Refael, and V. Galitski, Floquet topological insulator in semiconductor quantum wells, *Nat. Phys.* **7**, 490 (2011).
- [84] M. S. Rudner and N. H. Lindner, Band structure engineering and non-equilibrium dynamics in Floquet topological insulators, *Nat. Rev. Phys.* **2**, 229 (2020).
- [85] I. Mondragon-Shem, T. L. Hughes, J. Song, and E. Prodan, Topological criticality in the chiral-symmetric AIII class at strong disorder, *Phys. Rev. Lett.* **113**, 046802 (2014).
- [86] E. J. Meier, J. Ang’ong’a, F. A. An, and B. Gadway, Observation of the topological Anderson insulator in disordered atomic wires, *Nature* **565**, 337 (2019).
- [87] S. Rachel, Interacting topological insulators: a review, *Rep. Prog. Phys.* **81**, 116501 (2018).
- [88] S. Yao and Z. Wang, Edge states and topological invariants of non-Hermitian systems, *Phys. Rev. Lett.* **121**, 086803 (2018).
- [89] K. Kawabata, K. Shiozaki, M. Ueda, and M. Sato, Symmetry and topology in non-Hermitian physics, *Phys. Rev. X* **9**, 041015 (2019).
- [90] Y. Ashida, Z. Gong, and M. Ueda, Non-Hermitian physics, *Adv. Phys.* **69**, 249 (2020).
- [91] M. Atala, M. Aidelsburger, J. T. Barreiro, D. Abanin, T. Kitagawa, E. Demler, and I. Bloch, Direct measurement of the Zak phase in topological Bloch bands, *Nat. Phys.* **9**, 795 (2013).
- [92] E. J. Meier, F. A. An, and B. Gadway, Observation of the topological soliton state in the Su–Schrieffer–Heeger model, *Nat. Commun.* **7**, 13986 (2016).
- [93] M. Lohse, C. Schweizer, O. Zilberberg, M. Aidelsburger, and I. Bloch, A Thouless quantum pump with ultracold bosonic atoms in an optical superlattice, *Nat. Phys.* **12**, 350 (2016).
- [94] S. Nakajima, T. Tomita, S. Taie, T. Ichinose, H. Ozawa, L. Wang, M. Troyer, and Y. Takahashi, Topological Thouless pumping of ultracold fermions, *Nat. Phys.* **12**, 296 (2016).
- [95] V. D. Pham, Y. Pan, S. C. Erwin, and S. Fölsch, Quantum dots on the InAs(110) cleavage surface created by atom manipulation, *Phys. Rev. Research* **6**, 013269 (2024).
- [96] V. D. Pham, Y. Pan, S. C. Erwin, F. v. Oppen, K. Kanisawa, and S. Fölsch, Topological boundary states in engineered quantum-dot molecules on the InAs(111)A surface: Odd numbers of quantum dots, *Phys. Rev. Research* **6**, 033268 (2024).
- [97] A. Blanco-Redondo, I. Andonegui, M. J. Collins, et al., Topological Optical Waveguiding in Silicon and the Transition between Topological and Trivial Defect States, *Physical Review Letters* **116**, 163901 (2016).
- [98] M. C. Rechtsman, J. M. Zeuner, Y. Plotnik, et al., Photonic Floquet topological insulators, *Nature* **496**, 196–200 (2013).
- [99] D. Xie et al., Topological characterizations of an extended Su–Schrieffer–Heeger model, *npj Quantum Inf.* **5**, 55 (2019).
- [100] O. Gröning et al., Engineering of robust topological quantum phases in graphene nanoribbons, *Nature (London)* **560**, 209 (2018).
- [101] Z. Yang, F. Gao, X. Shi, X. Lin, Z. Gao, Y. Chong, and B. Zhang, Topological acoustics, *Phys. Rev. Lett.* **114**, 114301 (2015).
- [102] W. S. Bakr, J. I. Gillen, A. Peng, S. Fölling, and M. Greiner, A quantum gas microscope for detecting single atoms in a Hubbard-regime optical lattice, *Nature* **462**, 74–77 (2009).
- [103] S. Porta, N. T. Ziani, D. M. Kennes, F. M. Gambetta, M. Sassetti, and F. Cavaliere, Effective metal-insulator nonequilibrium quantum phase transition in the Su–Schrieffer–Heeger model, *Phys. Rev. B* **98**, 214306 (2018).
- [104] F. Liu, Analytic solution of the  $n$ -dimensional Su–Schrieffer–Heeger model, *Phys. Rev. B* **108**, 245140 (2023).